CrossMark

REGULAR PAPER

Thangadurai Murugan · **Chandrala Lakshmana Dora** · **Sudipta De** · **Debopam Das**

A comparative three-dimensional study of impulsive flow emanating from a shock tube for shock Mach number 1.6

Abstract A three-dimensional transient impulsive flow emanating from an open end of a 165-mm driver section shock tube is investigated numerically in the present study for a shock Mach number of 1.6. Here, the main objective was to find out an appropriate model to simulate the early evolution of the high Mach number transient flows by comparing the flow field obtained from two numerical models with both qualitative and quantitative experimental observations. The 3-D numerical simulations were performed by solving RANS equations using the shear stress transport K-ω model and large eddy simulation of the flow with the help of ANSYS CFX software. The experiments were performed with the simultaneous 2-D and 3-D particle image velocimetry systems and high-resolution smoke flow visualizations. The 2-D PIV results were used for comparing the numerical results obtained on a plane, and the 3-D PIV results were used to compare the azimuthal variations across the vortex ring. It is observed that the velocity field of the transient jet, Kelvin–Helmholtz (K–H) vortices at the trailing jet and the interaction of K–H vortices with the primary vortex ring were resolved well in LES quite similar to the experiments. However, the SST K-ω model resolved only the velocity field of the transient jet in the axial region similar to the experiments and dissipated the K–H vortices at the jet boundary. Though both models resolved the shear layer originated from the triple point, they did not predict the rollup and formation of vortices and their interactions observed in a 24 MP camera. This demands the use of a higher spatial resolution. It is also noticed that a substantial adverse pressure gradient experienced by the vortex ring and trailing jet during the early stage of evolution due to the presence of precursor/incident shock was responsible for the pairing up and merging of the shear layer vortices to form a stronger counter-rotating vortex ring. This adverse gradient also plays a dominant role in the azimuthal expansion (rapid increase in diameter) of the vortex ring.

Keywords 3-D simulation · Compressible vortex ring · SST K-ω model · LES · PIV · Transient under-expanded jet

1 Introduction

Knowledge of shock diffraction and the three-dimensional characteristics of the ensuing under-expanded jets for different shock Mach numbers (M) is essential for designing the silencers used in the firearms. The silencers minimize the noise produced by the muzzle blast where the expulsion of propellant gases creates an impulsive under-expanded jet (Phan and Stollery 1983). The understanding of impulsive jets is also

T. Murugan (✉) · S. De
Central Mechanical Engineering Research Institute (CSIR), Durgapur, India
E-mail: murugan.thangadurai@gmail.com

C. L. Dora · D. Das
Indian Institute of Technology, Kanpur, India

critical in designing the pulse detonation engines (Kailasanath 2003), micro-jets, synthetic jets (Murugan et al. 2016a, b) and plasma actuators (Zhang et al. 2016). The knowledge of flow expansion at the shock tube exit is also vital in designing the blast wave generators for studying the blast wave interaction with objects (Murugan et al. 2017).

The two-dimensional (2-D)/axisymmetric characteristics of impulsive flows originating from the shock tube for M up to 1.5 were reported in many earlier experimental studies (Baird 1987; Brouillette and Hebert 1997; Arakeri et al. 2004; Kontis et al. 2006; Murugan 2008), where the optical techniques such as shadowgraph and schlieren, smoke flow visualizations and 2-D particle image velocimetry (PIV) were used. However, it is challenging to obtain an accurate velocity field through PIV at higher M ($\geq$ 1.5) due to the presence of a Mach disk and an embedded shock in the axial region (Zare-Behtash et al. 2008; Murugan et al. 2012). Moreover, the velocity field obtained from PIV deviates from the actual values behind the embedded shock due to finite particle tracer relaxation length (Murugan et al. 2012). On the other hand, simultaneous velocity, density and pressure information with high spatial and temporal resolutions can be obtained from numerical simulations. However, the solver should be validated with the velocity field obtained in the shock-free regions and the shock cell structures obtained through optical techniques (Dora et al. 2014).

Many numerical studies on the impulsive jet at higher M were performed to understand the shock diffraction (Sun and Takayama 2003) and the evolution of shock cell structures by assuming the impulsive flow to be inviscid and axisymmetric (Ishii et al. 1999) at the early stage. However, the viscosity deviates the dynamics of vortices during the later stage of vortex ring evolution (Murugan et al. 2013, 2016a, b). The effect of low dissipation scheme (AUSM +) and the role of turbulence models (De and Murugan 2011) on planar impulsive jet was also addressed in the literature besides the validation of AUSM + scheme with PIV results for $M < 1.5$. However, the appearance of Kelvin–Helmholtz (K–H) instability on the shear layer originating from the triple point on the Mach disk makes the flow highly complicated at $M \geq 1.6$ (Dora et al. 2014).

The smoke flow visualizations reported in the previous studies (Murugan 2008; Dora et al. 2014) have revealed the asymmetrical formation of vortices in the shear layer originated from Mach disk and highly three-dimensional nature of the vortex ring at $M \geq 1.6$. This demands a 3-D simulation of impulsive flow for accurately predicting flow features at high M. Nevertheless, the results should be validated with the experiments either through PIV or optical techniques. The 3-D simulation of high M impulsive flows is computationally very expensive due to the wide range of turbulent structures present in the flow and their interactions with shock cell structures. Resolving all length scales of turbulence through direct numerical simulation is still quite impossible for this class of fluid flows, though an exponential growth of computational power is seen in recent times.

Zhang et al. (2014) examined a supersonic under-expanded jet for $M = 1.2$, 1.4 and 1.8 through 3-D simulation using LES with the combination of high-order hybrid schemes. They showed the trajectories of the primary and secondary vortex ring (SVR) and observed the evolution of SVR similar to the one shown by Murugan and De (2012). However, the transient flow from the shock tube and its 3-D characteristics were not discussed in the literature which is the main focus of the present study. Here, 3-D characteristics of the impulsive jet generated from a 165-mm driver section length shock tube are investigated numerically by solving the Reynolds-averaged Navier–Stokes equations (RANS) with shear stress transport (SST) K-ω model and large eddy simulation (LES) of the flow using ANSYS CFX for PR = 10. The incident shock Mach number (M) corresponds to PR = 10 was 1.6. The numerical results were validated with the 2-D and 3-D PIV results obtained for the same pressure ratio and driver section length besides the high-resolution smoke flow visualizations.

2 Discretization domain and computational procedure

The computational domain was divided into a shock tube interior and exterior zones and Fig. 1 shows the isometric and side view of the same. The driver and driven section length of the shock tube were 165 and 1200 mm, respectively. The inner diameter of the shock tube was 64 mm, and the thickness of the shock tube was 2.61 mm. These shock tube dimensions were chosen to compare the numerical data with the experimental results. The outside domain has a length and diameter of 1500 and 1000 mm, respectively. A total number of 11.4 million hexahedra elements were used in the present simulation. The grids were uniformly distributed in the azimuthal direction. Finer grids were used close to the exit and at the shock tube
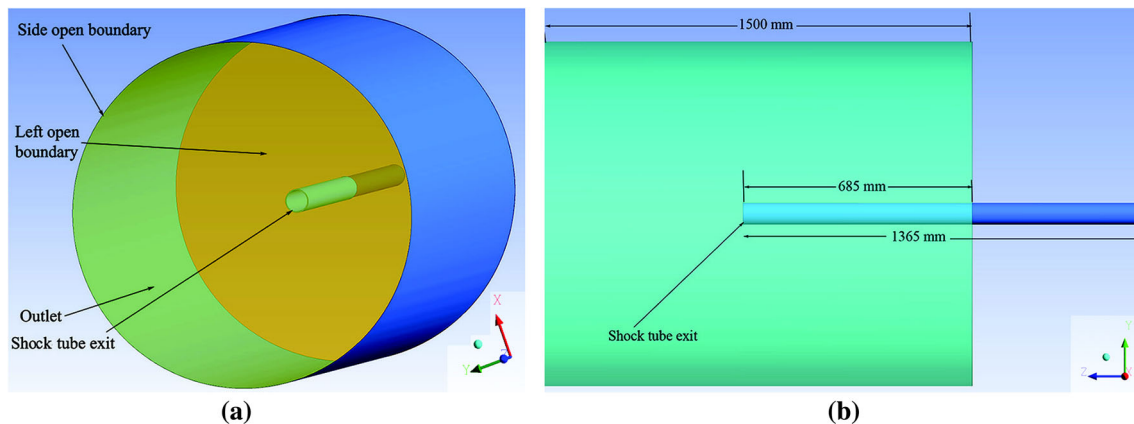
Fig. 1 **a** Front **b** side views of the Computational domain with shock tube

end wall. Grids were stretched away from the end wall and at the exit of the shock tube (Z). The smallest grid size was 0.47 mm.

The RANS equations with SST K-ω model equations and the filtered Navier–Stokes equations with LES model were solved along with continuity, energy and state equations. The shock tube driver section was initialized with ten times the ambient pressure, and an ambient pressure of 1.01325×105 N/m^2 was used in other zones. The initial temperature was kept uniform (300 K) throughout the computational domain. Air was used as a working fluid with a specific heat ratio (γ) of 1.4. The inner and outside shock tube walls were considered with no-slip boundary condition. The open boundaries were treated with non-reflecting boundary condition.

3 Experimental setup and instrumentation

The schematic of the experimental setup with 2-D and 3-D PIV arrangements is shown in Fig. 2. The driver and driven section length of the shock tube were similar to the dimensions shown in Sect. 2. The inner and outer diameters of the shock tube were 64 and 100 mm, respectively. A straight nozzle with chamfer angle of 60° was attached (Dora et al. 2014) at the exit to ensure a smooth roll up of the vortex sheet, and it was used to make a sharp edge similar to the numerical simulation at the shock tube exit. More details about the experimental procedure and instrumentation were given in Murugan et al. (2012). Mylar sheets were used as a diaphragm, and they were ruptured using a pneumatic plunger. Three flush-mounted piezoelectric pressure transducers were installed in the driven section for measuring the shock speed. The pressure data were acquired at a sampling rate of 2 MS/s using NI PCI-6133 data acquisition card. The synchronizer receives the trigger signal from the pressure transducer kept 200 mm inside the shock tube.

The experiments were conducted in two stages; simultaneous smoke flow visualizations were performed in two orthogonal planes in the first stage. The flow was illuminated by two 200 mJ/pulse Nd/YAG lasers, and the laser sheets were arranged perpendicular to each other as shown in Fig. 2. The thickness of the laser sheet was 1 mm. The 2-D and 3-D PIV measurements were performed on these two planes in the second stage. The 3-D PIV was performed in plane A in the azimuthal direction with two CMOS cameras (1024×1280 pixels) fixed on a motorized traverse with Scheimpflug mounts. The angle between two cameras was set at 80° for achieving high resolution in out-of-plane velocity component. The 2-D PIV was employed on the horizontal plane (B) with a CCD camera of resolution 2048×2048 pixels. The time between the laser pulses in 2-D and 3-D PIV measurements was fixed at 5 and 1 μs, respectively. The image processing was performed using a multi-grid cross-correlation algorithm, and an interrogation area of 32×32 pixels was used for calculating the velocity field. Thirty experiments were performed with the same experimental conditions, and the observed maximum variation in shock speed was 1%. Similarly, the maximum deviation in vortex ring position was found to be less than 0.5%.
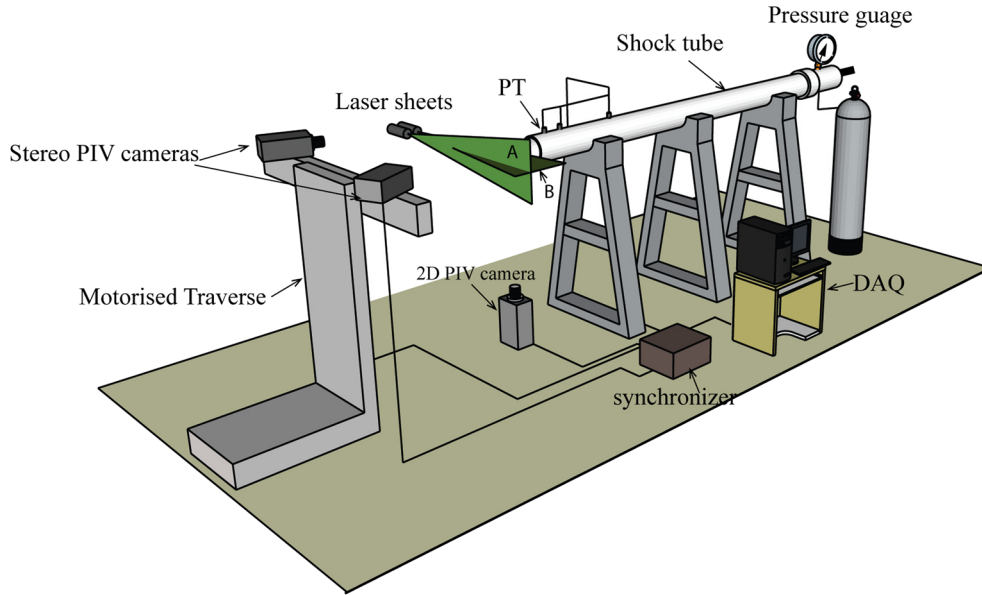
Fig. 2 Experimental set up for a simultaneous 2-D and 3-D PIV measurements outside the shock tube exit

4 Results and discussion

At first, the smoke flow visualizations showing the evolution of the high *M* impulsive jet obtained with a 24 MP camera are discussed. These images show the evolution of Mach disk and shear layer vortices originated from the triple point more clearly than the earlier visualizations (Murugan 2008; Murugan and Das 2010). The velocity data obtained at a sectional plane of the jet from SST K-ω and LES models are compared with 2-D PIV results in the next section. It is followed by the comparison of velocity data along the axis and across the vortex obtained from both PIV and numerical models. At last, the vorticity fields obtained at a sectional plane from LES and SST models are shown to illustrate the quantitative changes in the flow field. Next section showed the comparison of vorticity fields obtained from models at different azimuthal planes with the azimuthal flow visualizations and 3-D PIV results. Finally, the static pressure data obtained from models along the axis during the evolution of the jet were used along with flow visualizations for
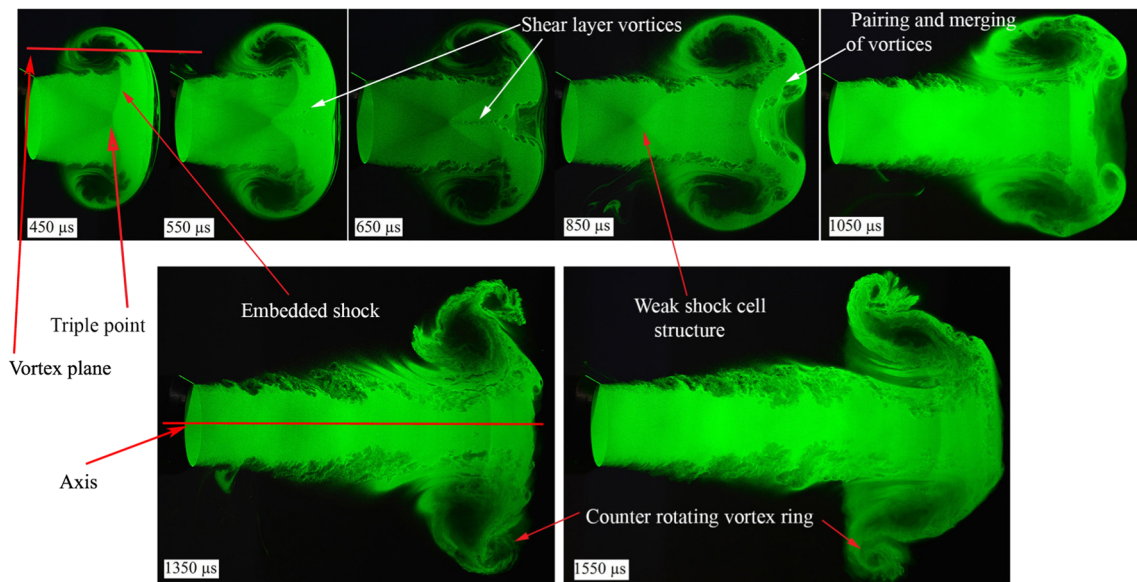

**Fig. 3** Smoke flow visualizations show the evolution of shock cell structures and shear layer vortices

determining the role of adverse pressure gradient generated by the incident shock on the shear layer vortices formation and the spreading of the jet in the azimuthal direction.

4.1 Evolution of Mach disk and the subsequent shear layer vortices

Figure 3 shows the development of transient impulsive jet obtained at different times using a 24 MP camera. These images are captured by illuminating the seeded smoke particles using the 200 mJ/pulse Nd/YAG laser similar to the earlier studies (Murugan 2008; Murugan and Das 2010). As the initial development of shock cell structures and vortex ring for $t < 450$ µs was discussed elaborately in other studies (Murugan and De 2012; Murugan et al. 2013), the evolution of shock cell structures and the tiny vortices created on the shear layer originating from the triple point is clearly shown in Fig. 4 by magnifying the flow in the axial region in Fig. 3. Here, $t = 0$ is taken when the incident shock reaches the shock tube exit. At $t = 450$ µs, the formation of Mach disk from the embedded shock is initiated (Murugan and De 2012) and this causes the formation of a weak shear layer from the triple point which is difficult to observe from the particle image. However, the presence of tiny vortices at the shear layer is observed at $t = 500$ µs and 550 µs.

These vortices are generated due to the Kelvin–Helmholtz (K–H) instability occurring at the shear layer. They grow in size, get paired and merged as they evolve (Rikanati et al. 2006) which is seen at $t = 650$ µs and 750 µs. The strength of the Mach disk reduces when the pressure inside the shock tube falls below a critical value (Dora et al. 2014). This causes a reduction in the height of the Mach disk and the
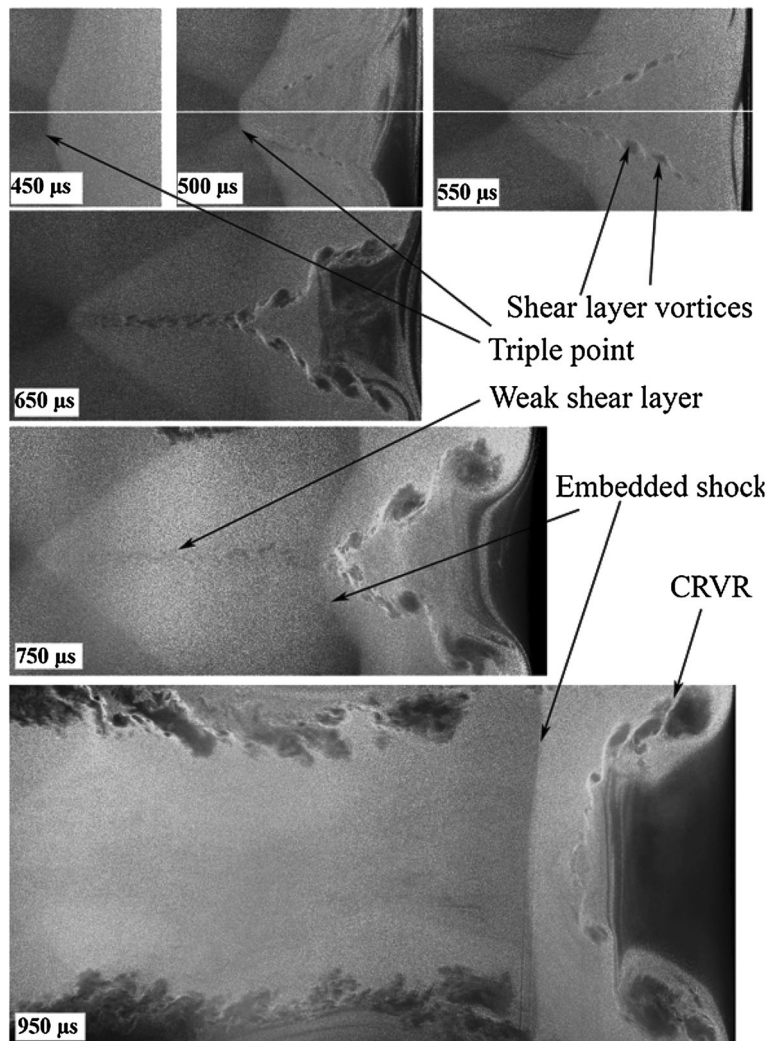
Fig. 4 Magnified view of shock cell structures, Mach disk and shear layer vortices
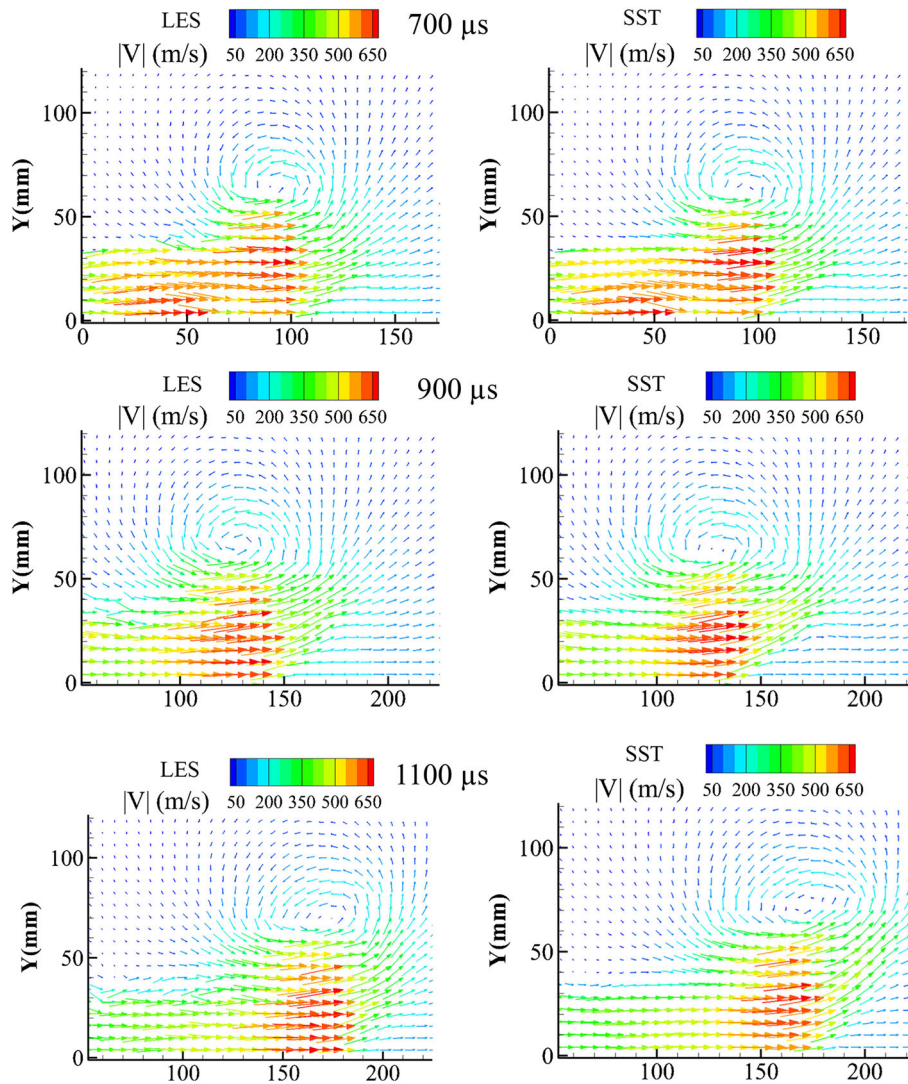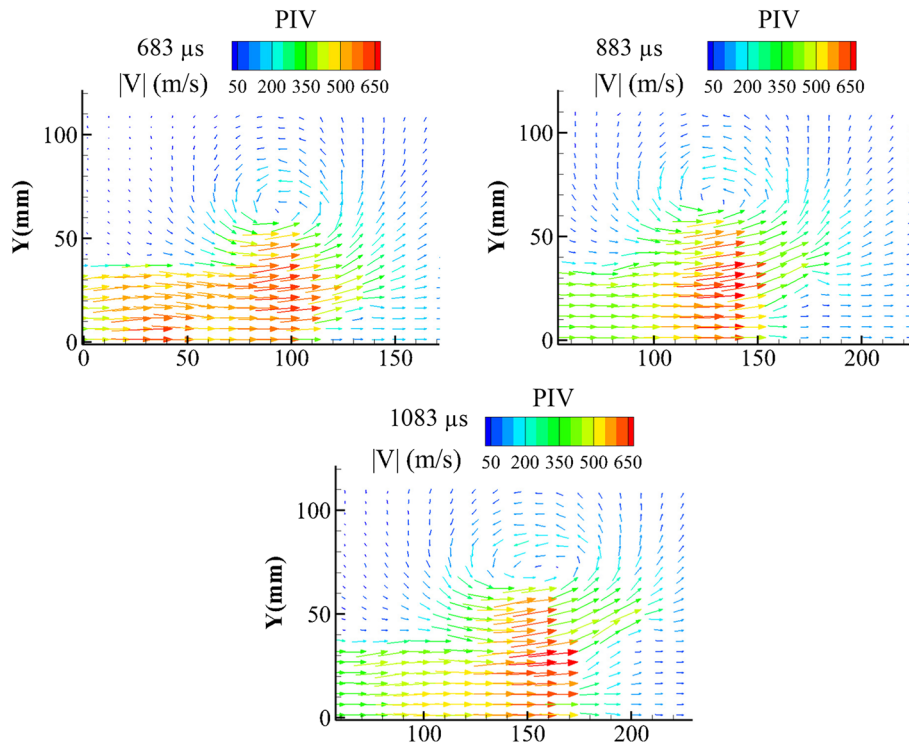
Fig. 5 Comparison of velocity field obtained from LES and SST models at three times

disappearance of shear layer originating from the triple point ($t = 750$ μs). Both Mach disk and shear layers are disappeared in the axial region at $t = 750$ μs. The shear layer vortices generated at earlier times have merged and formed the counter-rotating vortex ring (CRVR) ahead of the vortex ring at $t = 1050$ μs. Though the shock cell structure is symmetrical, the formation of shear layer vortices and eddy pairing is asymmetrical in Fig. 4 at $t = 550$ μs and 650 μs. Further, the shear layer vortices at the jet boundary and their penetration into the vortex core were also asymmetrical. These cause the vortex ring to develop three-dimensionality during growth and translation along the downstream direction.

4.2 Comparison of velocity fields of the impulsive jet

Figure 5 shows the sectional velocity field of the impulsive jet obtained from LES and SST models at $t = 700$, 900 and 900 μs, respectively. Figure 6 shows the velocity field data obtained through 2-D PIV at times close to the numerical results. It is difficult to get the same time in experiments due to the changes in the ruptured area of the diaphragm which alters the shock speed. Since the trigger signal to capture the PIV images was obtained from a pressure transducer kept 200 mm inside the shock tube, any change in shock speed creates a difference in time. A variation in shock speed within a range of $\pm$ 10 M/s was observed in the experiments for the incident shock speed of 555 M/s due to non-uniform rupturing of the diaphragm. The number of velocity vectors in the numerical simulations was limited to match with the experiments as
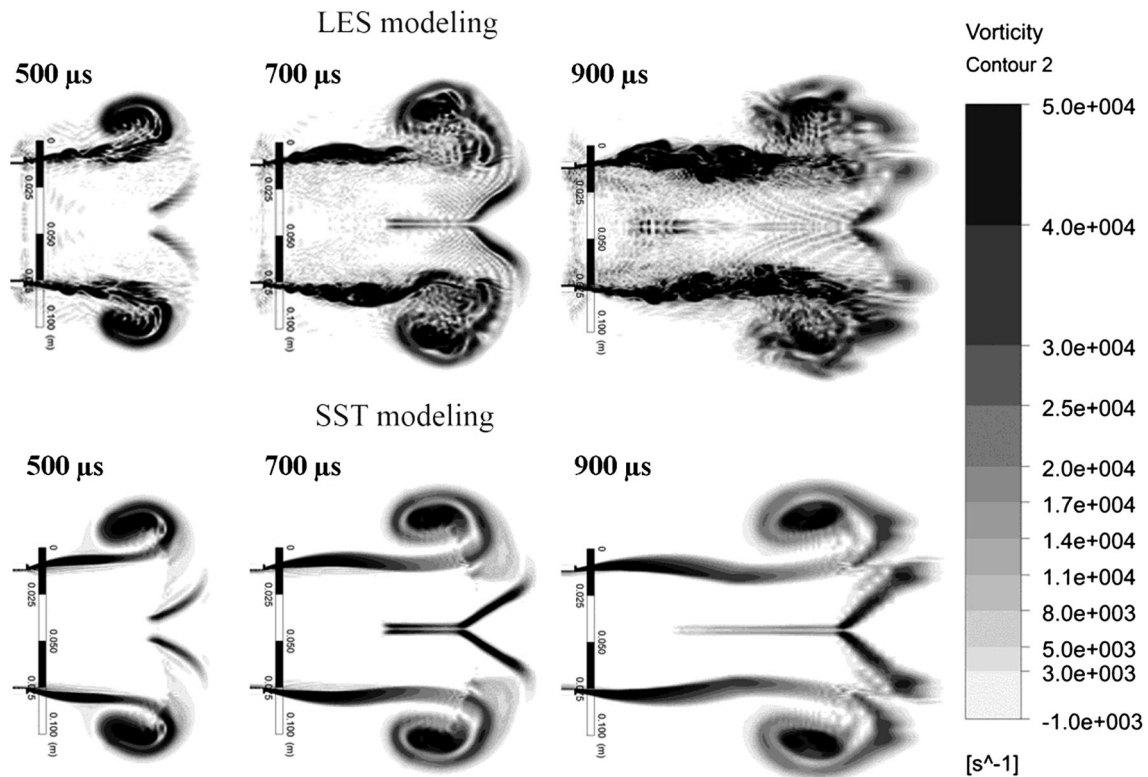
Fig. 6 Velocity field of impulsive jet obtained from PIV at three different times
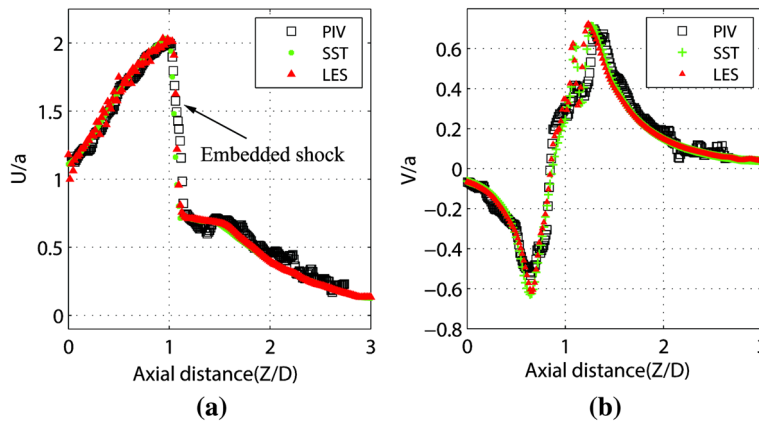
Fig. 7 Comparison of **a** axial velocity and **b** velocity across the vortex with PIV results

the 2-D PIV was performed with a 2 MP camera. Further, the velocity contour levels were also kept same in both simulations and experiments for a better comparison. The magnitudes of velocity field obtained inside the impulsive jet and vortex ring were almost same in LES and SST models, and they were closely matched with the 2-D PIV velocity data in Fig. 6. Further, the velocity data across the embedded shock were predicted well in models compared to 2-D PIV. Here, the accumulation of particles behind the embedded shock in PIV causes some variations in velocity. The LES has resolved velocity fluctuations at the trailing jet to some extent compared to the SST model which dissipated these fluctuations.

Figure 7 shows the velocity data extracted along the axis and the vortex plane (Fig. 3) from SST and LES models and 2-D PIV at $t = 430$ μs. Here, U and V are axial and lateral velocities. The axial distance and the shock tube inner diameter are denoted by Z and D, respectively. $Z = 0$ denotes the shock tube exit. The non-dimensional velocity along the axis (shown in Fig. 3 at t = 1350 μs) increased with an increase in distance and reached $M \sim 2$ at $Z/D \sim 1$ in Fig. 7a due to the expansion of under-expanded jet at the shock

Fig. 8 Evolution of the impulsive jet obtained from LES and SST modeling

tube exit. The formation of Mach disk after $Z/D = 1$ decelerates the velocity ahead of the vortex ring. The SST results matched closely with PIV between the shock tube exit and embedded shock whereas LES showed some fluctuations due to the presence of large-scale vertical structures.

Both LES and SST showed similar trend ahead of the embedded shock, however, PIV showed a higher drop in velocity which resulted from a higher particle density. Figure 7b shows the variations of lateral velocity across the vortex plane shown in Fig. 3 at $t = 450$ μs. Here, the lateral velocity is zero at the center of the core, and it increases to a maximum velocity at the edge of the vortex core. The velocity data obtained from models are matching quite well with the PIV except in the forward region of the vortex ring ($Z/D > 1.2$) where the shear layer vortices generated at the jet boundary of the trailing jet penetrate into the vortex core (Fig. 3; Murugan 2008). The LES has resolved the penetration of these vortices near the edge of the core instantaneously with the use of filtered N-S equations, and the SST has shown a thick shear layer entering into the core (Fig. 8). Since the PIV was performed with a 2 MP camera which did not have higher spatial resolutions in the vortex region (Fig. 6), it deviates from the numerical results.

Figure 8 shows the vorticity field of the impulsive jet obtained at $t = 500$, 700 and 900 μs using LES and SST models. Here, the vorticity contour levels are kept same in LES and SST models for comparing the vortices and shear layers in the flow field. The LES model has resolved the shear layer vortices and their interactions at the jet boundary. The size of these vortices is small in smoke flow visualizations in Fig. 3 and earlier study (Dora et al. 2014). The SST model did not capture these trailing jet vortices and showed a strong shear layer at the jet boundary by dissipating the fluctuations. The shear layer originating from the triple point at the Mach disk is resolved well in both the models at the early stage ($t \leq 500$ μs). The formation of tiny vortices, their pairing up and merging observed through flow visualizations (Fig. 4) at later stages are not resolved in models, and laminar shear layers are noticed in the axial region. However, the formation of counter-rotating vortex ring resulting from the interaction of shear layer/tiny vortices produced from the triple point with another shear layer resulted from an interaction of the reflected shock with embedded shock (Murugan and De 2012; Zhang et al. 2014) is predicted well in models. Though LES has shown some large-scale structures inside the jet and the shear layer in the axial region compared to SST at $t = 900$ μs, a higher spatial resolution is needed for LES to resolve these tiny vortices formation at early stages observed through visualizations (Fig. 4).
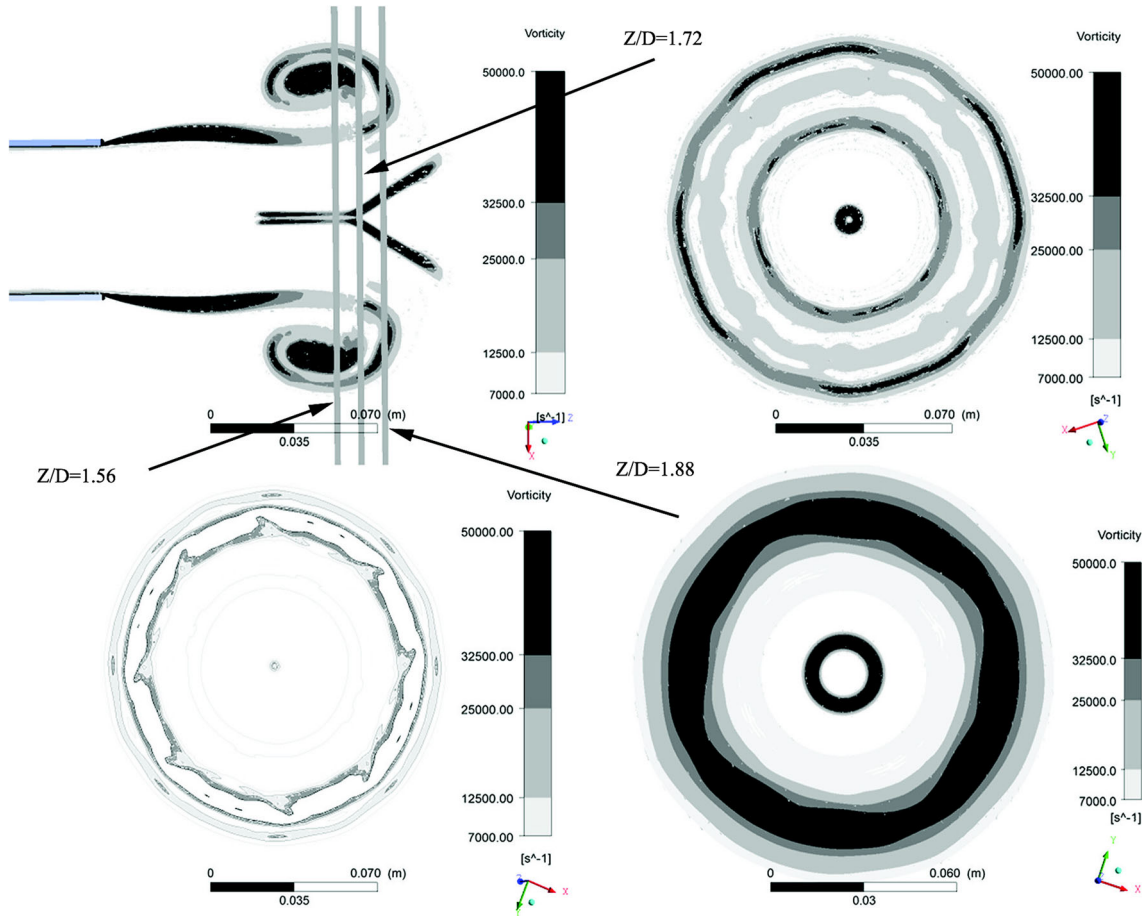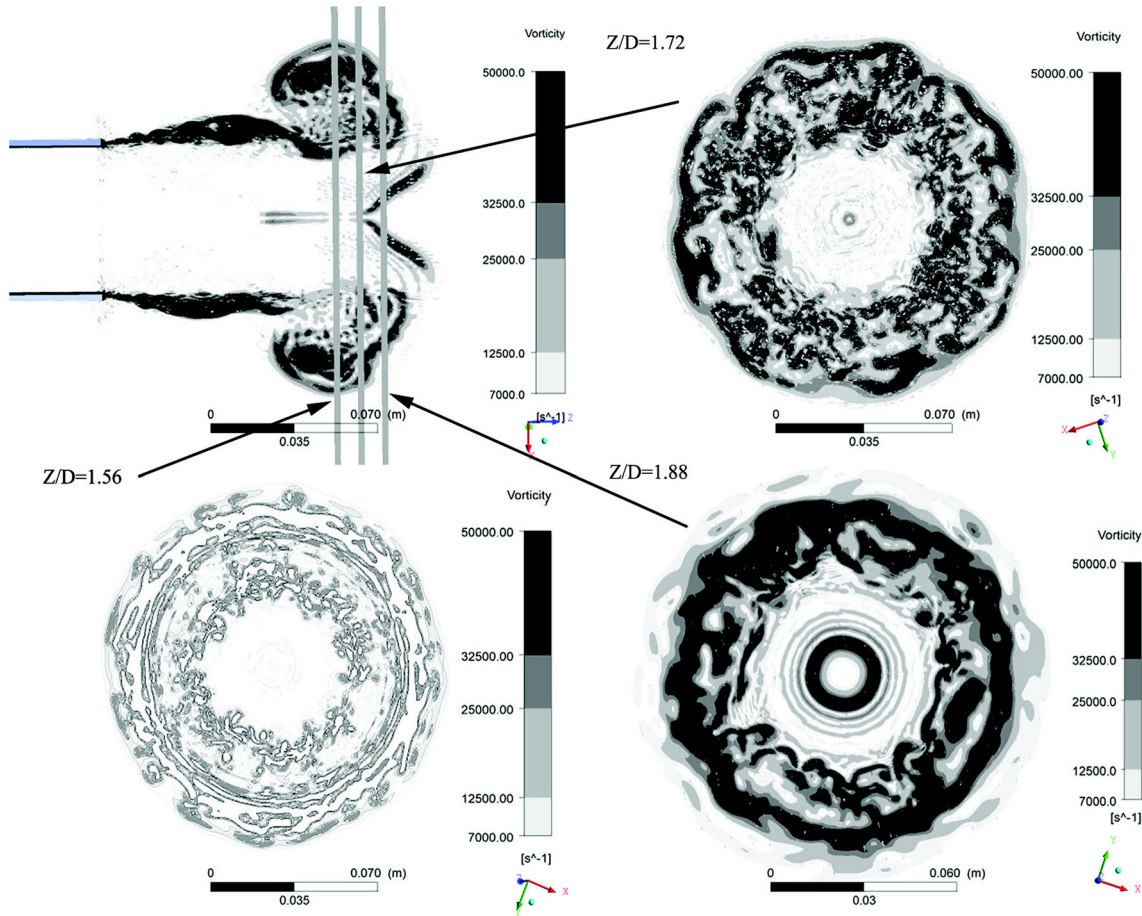
Fig. 9 Variation of vorticity field obtained from SST model at three azimuthal planes

4.3 Comparison of azimuthal variations inside the vortex ring

Figures 9 and 10 show the vorticity field obtained through SST and LES models at a sectional plane of the impulsive jet at $t = 700$ μs and three azimuthal planes of the vortex ring at $Z/D = 1.56$, 1.72 and 1.88. Here, these planes are chosen to show the 3-D nature of the vortex core, shear layer generated at the triple point and the penetration of vortices generated at the jet boundary into the vortex core. The sectional view of the impulsive jet obtained from SST model shows a strong shear layer at the periphery of the jet which suggests that it is not capable of resolving the K–H vortices observed in smoke flow visualizations (Fig. 3). This may be attributed to the fact that the SST model suppresses the fluctuations in the impulsive jet due to averaging and its stronger turbulent viscosity. However, LES resolved these vortices, but the size of the vortices is larger compared to flow visualizations in Fig. 10 and Dora et al. (2014).

The azimuthal view of vortex ring obtained at $Z/D = 1.56$ in Fig. 9 shows discrete structures along the inner periphery of the vortex core. These structures may induce instabilities to make the vortex ring completely turbulent at the later stage (Murugan 2008). The presence of these structures is felt in other planes at the edge of the vortex core, and significant undulations are seen in the jet boundary shear layer at $Z/D = 1.88$. The shear layer originated from the Mach disk is smooth without any variation in azimuthal direction at all three planes. The LES shows a completely 3-D flow field at all three azimuthal planes in Fig. 10. This is due to the inherent property of the LES to resolve the large-scale eddies from velocity fluctuations. The entrainment of K–H vortices formed at the jet boundary into the primary vortex ring and their strong interaction with other vortical structures having different wave numbers makes the vortex core fully three dimensional.

The symmetrical structure of the impulsive jet observed in low Mach numbers (Murugan 2008) is no longer recognized, and the flow field is governed by eddies of different frequencies and length scales.

Fig. 10 Variation of vorticity field obtained from LES at three azimuthal planes

However, the shear layer originated from the triple point is almost similar to SST model though small undulations are noticed. This demands a higher spatial resolution to resolve these vortices which will be done in future. Figure 11 shows the azimuthal flow visualizations obtained at two planes in the left frame, and the lateral velocity field at the corresponding planes obtained through 3-D PIV in the right frame. Both these qualitative and quantitative images show severe three dimensionalities in the azimuthal plane. A higher resolution in velocity data in the azimuthal plane may show the shear layer in the axial region and the jet velocity field more accurately which will be performed in future with a higher-resolution camera rather than a 4 MP camera.

4.4 Variations of centerline static pressure and their consequences

Figure 12 shows the variation of instantaneous static pressure obtained along the axis during the evolution of the impulsive jet from LES and SST models. Here, the x-axis is given from $Z/D = -2$ to 6 to emphasize the changes in pressure occurring inside the shock tube where $Z/D = 0$ represents the shock tube exit. Both SST and LES models show a similar trend in axial pressure variations except at $t \sim 100$ μs. Here, the incident shock produced through LES is behind by $Z/D = 0.15$ compared to SST model. Hence, the incident shock strength is higher in LES compared to the SST model as the strength of the incident shock decreases exponentially after diffraction. Since the incident shock wave was propagating through the driven section of the shock tube having a length of 1200 mm, it is quite likely that two different numerical schemes will result in different wave locations (Trefethen 1982).

The subsonic flow behind the incident shock gradually reaches to sonic velocity at the shock tube exit after diffraction of incident shock due to flow expansion resulting from the pressure imbalance between the fluid inside the shock tube and ambient ($p/p_a \sim 3$). Here, the disturbance waves travel inside the shock tube
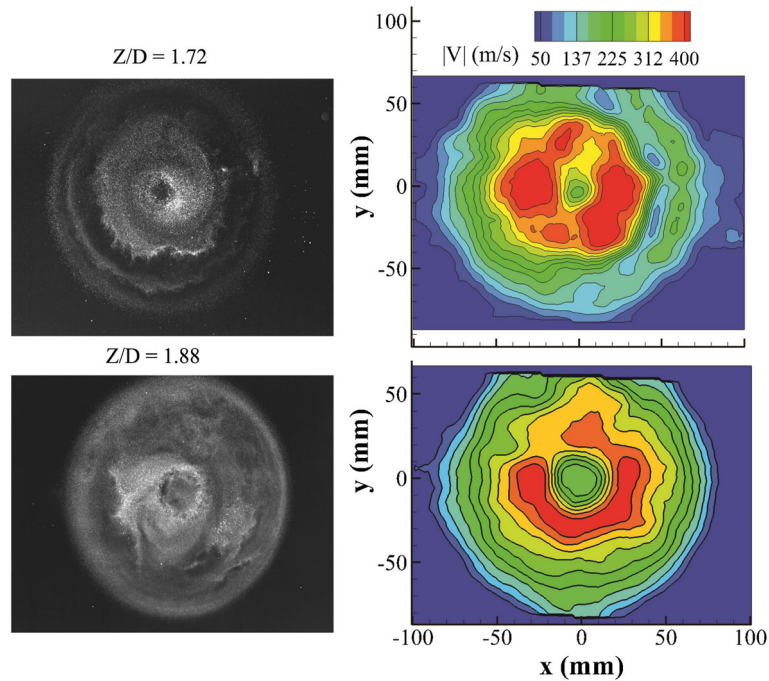
Fig. 11 Azimuthal flow visualizations at two planes and their corresponding lateral velocity field obtained through 3-D PIV

till the exit velocity reaches sonic condition ($M = 1$). A drop in pressure at the shock tube exit from 2.55 at $t = 100$ µs to 2 at $t = 300$ µs reflects the propagation of disturbance waves inside the tube and expansion flow. The impulsive jet outside the shock tube exit reaches supersonic velocity due to the Prandtl–Meyer expansion fan at the outer edge of the shock tube exit. The pressure at the exit remains constant (p/pa $\sim$ 2) once the sonic condition is reached ($t = 100$ and 500 µs) until otherwise, the pressure inside the shock tube reduces ($t \geq 700$ µs).

The formation of embedded shock and the subsequent development of Mach disk were discussed in many earlier studies (Murugan and De 2012). A substantial adverse pressure gradient (p/pa $\sim$ 1.4) is noticed in the region between the incident shock and the Mach disk at $t = 300$ µs, and it is continued to exist up to $t = 500$ µs. This adverse pressure gradient plays a major role on the formation of Mach disk in the axial region (Fig. 4). The embedded shock attached to the vortex ring transformed into a reflected shock at the triple point as the vortex ring evolves along the downstream direction. The shock cell structure development and the shear layer originated at the triple point of the Mach disk were clearly shown in Dora et al. (2014) through simulations which were not seen in the particle image at Fig. 4. However, the formation of tiny vortices at the shear layers is clearly seen in Fig. 4 due to the solid body rotation of the vortices' core. The pressure plots up to $t = 700$ µs clearly suggest that the combined action of the adverse pressure gradient generated behind the incident shock and the supersonic expansion at the exit are responsible for the roll up, formation, pairing up and merging of the tiny vortices besides the K–H instability. Further, this adverse gradient is also responsible for the merged vortices to form a counter-rotating vortex ring ahead of the vortex ring (Fig. 4) and a huge increase in diameter of the vortex ring observed by Murugan (2008).

The adverse pressure gradient ahead of the embedded shock is significant up to $t = 900$ µs in the present case, and it reduces gradually as the incident shock races away along the downstream direction due to a pseudo-spherical expansion of the incident shock. The non-dimensional pressure at the exit reduces continuously once the expansion waves reflected from the end wall of the driver section reaches the shock tube exit. A continuous reduction in pressure at $Z/D = 0$ from $t = 900$ µs is due to the arrival of expansion waves at the exit.
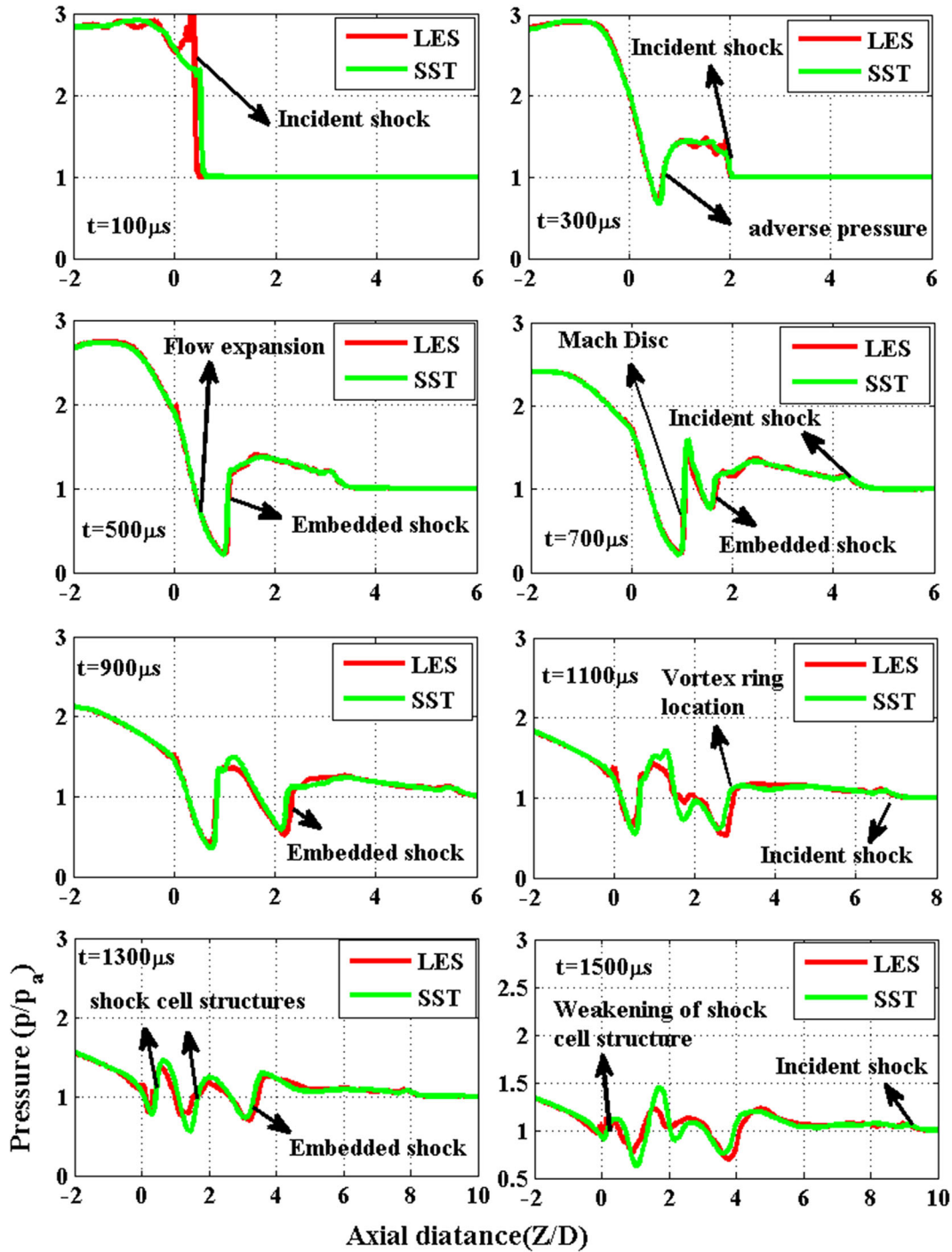
Fig. 12 Variation of non-dimensional static pressure along the axis obtained from LES and SST models

5 Conclusions

Three-dimensional simulations of impulsive flow emanating from an open end of a 165-mm driver section shock tube have been performed using RANS based SST K-ω and LES models for a shock Mach number of 10. They have been validated with the sectional and azimuthal vorticity fields obtained from smoke flow visualizations, 2-D and 3-D particle image velocimetry. It was observed from experiments that the primary vortex ring and the subsequent trailing jet exhibit severe three-dimensionality after the formation of

embedded shock in the axial region. The tiny vortices formed at the shear layer originated from the triple point and their subsequent pairing up and merging were responsible for this three-dimensionality in the flow field. It is observed that the LES resolved the K–H vortices at the periphery of the trailing jet and their interaction with the primary vortex ring quite similar to the experiments. The other large-scale structures existing inside the impulsive jet do not contribute significantly to the 3-D nature of the vortex ring. This suggested that the K–H vortices at the jet boundary play a dominant role in the turbulent nature of the primary vortex ring. The velocity field obtained at the section planes showed that the trailing jet flow obtained from SST was matched well with the 2-D PIV results compared to LES except for the jet boundary.

The calculation of static pressure along the axis had revealed that the adverse pressure gradient experienced by the impulsive jet was responsible for the enhancement in merging of shear layer vortices, formation of counter-rotating vortex rings and rapid increase in vortex ring diameter in the azimuthal direction observed by Murugan (2008). The presence of incident shock in the vicinity of primary vortex ring during early evolution caused the adverse pressure gradient. The formation of vortices at the shear layer originated from the Mach disk, their pairing, and merging was not resolved in either the SST or LES models. A higher spatial resolution might capture these small-scale vortices rollup and merging. Further, the smoke flow visualizations and PIV recorded only the integrated smoke density and velocity information. There is a possibility that the three-dimensional perturbations at the small vortices may not show up on integrated images. Capturing the instantaneous images with lesser exposure time in experiments may reveal smaller vortices and their merging. Often it is postulated that the numerical schemes create spurious non-physical vortices, which are to be smoothed by a turbulence model. However, a second-order accurate Euler and Navier–Stokes results of vortices resulting from Kelvin–Helmholtz instability matched well with the experimental visualization and the use of a turbulence model suppressed these vortices (Rubidge and Skews 2014). Here, the results obtained from LES, SST K-ω models and their comparison with PIV have revealed that the LES model is best suited for predicting detailed flow field with vortices formations and their interaction. This will be essential in identifying the small- and large-scale turbulence noise. The SST model is good for obtaining the shock cell structures and the mean flow characteristics of the jet which is useful in quantifying the broadband shock associated noise.

References

Arakeri JH, Das D, Krothapalli A, Lourenco L (2004) Vortex ring formation at the open end of a shock tube: a PIV study. Phys Fluids 30:1008–1019

Baird JP (1987) Supersonic vortex rings. Proc R Soc Lond A 409:59–65

Brouillette M, Hebert C (1997) Propagation and interaction of shock generated vortices. Fluid Dyn Res 21:159–169

De S, Murugan T (2011) Numerical simulation of shock tube generated vortex: effect of numerics. I J Comput Fluid Dyn 25:345–354

Dora CL, Murugan T, De S, Das D (2014) Role of slipstream instability in the formation of counter-rotating vortex rings ahead of a compressible vortex ring. J Fluid Mech 753:29–48

Ishii R, Fujimoto H, Hatta N, Umeda Y (1999) Experimental and numerical analysis of circular pulse jets. J Fluid Mech 392:129–153

Kailasanath K (2003) Recent developments in the research on pulse detonation engines. AIAA J 41(2):145–159

Kontis K, An R, Edwards JA (2006) Compressible vortex ring studies with a number of generic body configurations. AIAA J 44:2962–2978

Murugan T (2008) Flow and acoustic characteristics of high Mach number vortex rings during evolution and wall-interaction: an experimental investigation. Ph.D. Thesis, Indian Institute of Technology, Kanpur

Murugan T, Das D (2010) Characteristics of counter-rotating vortex rings formed ahead of a compressible vortex ring. Exp Fluids 49:1247–1261

Murugan T, De S (2012) Numerical visualization of counter rotating vortex ring formation ahead of shock tube generated vortex ring. J Vis 15(2):97–100

Murugan T, De S, Dora CL, Das D (2012) Numerical simulation and PIV study of formation and evolution of compressible vortex ring. Shock Waves 22:69–83

Murugan T, De S, Dora CL, Das D, Premkumar P (2013) A study of the counter rotating vortex rings interacting with the primary vortex ring in shock tube generated flows. Fluid Dyn Res 45:025506

Murugan T, De S, Sreevatsa A, Dutta S (2016a) Numerical simulation of compressible vortex—wall interaction. Shockwaves 26(3):311–326

Murugan T, Deyashi M, Dey S, Rana SC, Chatterjee PK (2016b) A review on recent developments on synthetic jets. Def Sci J 66(5):489–498

Murugan T, De S, Kundu A, Sandhu IPS, Saroha DR (2017) interaction of a shock tube generated blast wave with solid obstacles. In: 11th international high energy materials conference & exhibits, 23–25 November, Pune, India

Phan KC, Stollery JL (1983) The effect of suppressors and muzzle brakes on shock wave strength. In: Proceedings of the 14th international symposium on shock tubes and waves, Springer Berlin, pp 123–129

Rikanati A, Sadot O, Ben-Dor G, Shvarts D, Kuribayashi T, Takayama K (2006) Shock-wave Mach-reflection slip-stream instability: a secondary small-scale turbulent mixing phenomenon. Phys Rev Lett 96:174503

Rubidge S, Skews B (2014) Shear-layer instability in the Mach reflection of shock waves. Shock Waves 24:479–488

Sun M, Takayama K (2003) Vorticity production in shock diffraction. J Fluid Mech 478:237–256

Trefethen LN (1982) Group velocity in finite difference schemes. SIAM Rev 24(2):113–136

Zare-Behtash H, Kontis K, Gongora-Orozcoc N (2008) Experimental investigations of compressible vortex loops. Phy Fluids 20:126105

Zhang H, Chen Z, Li B, Jiang X (2014) The secondary vortex rings of a supersonic under-expanded circular jet with low pressure ratio. Eur J Mech B Fluids 46:172–180

Zhang X, Huang Y, Wang X, Wang W, Tang K, Li H (2016) Turbulent boundary layer separation control using plasma actuator at Reynolds number 2000000. Chin J Aeronaut 29(5):1237–1246